Three-dimensional scaled boundary finite element method to simulate Lamb wave health monitoring of homogeneous structures: Experiment and modelling

Mohammad Ehsani [a,b], Mahnaz Shamshirsaz [a,*], Mojtaba Sadighi [b], Naserodin Sepehry [c], Richard Loendersloot [d]

[a] *New Technologies Research Center (NTRC), Amirkabir University of Technology, Tehran, Iran*
[b] *Mechanical Engineering Department, Amirkabir University of Technology, Tehran, Iran*
[c] *Faculty of Mechanical and Mechatronic Engineering, Shahrood University of Technology, Shahrood, Iran*
[d] *Dynamics Based Maintenance, Engineering Technology, University of Twente, Enschede, Netherlands*

ARTICLE INFO

ABSTRACT

Exploiting scattering and reflection related data of ultrasonic Lamb wave interactions with damage is a common approach to health monitoring of thin-walled structures. Using thin PZT sensors, the method can be implemented in real-time. Simulation of Lamb wave propagation and its interaction with damage plays an important role in damage diagnosis and prognosis. It is, however, a time-consuming task due to the high-frequency waves that are commonly used to detect tiny damage. The current study employs the Scaled Boundary Finite Element Method (SBFEM) for effective modeling of Lamb wave health monitoring of homogenous thin plates. The electrome-chanical effects of piezoelectric sensors are included in the model to improve accuracy and make the results comparable to those of laboratory experiments. Simple meshing of complex topologies is possible by converting standard finite elements to scaled boundary elements. The 3D SBFEM wave motion equations are solved in the time domain to capture the sensor's PZT response to a high-frequency tone-burst actuation. The results are validated by pitch-catch and pulse-echo laboratory tests carried out on thin plates. SBFEM is used to study wave propagation in complex configurations, such as a stiffened plate, and the results are compared to their FEM counterparts. According to the findings, SBFEM significantly reduces the computational costs associated with simulation of Lamb wave health monitoring while also providing significant accuracy in comparison to the experimental results.

1. Introduction

Structural Health Monitoring (SHM) is a rapidly developing technology that has a wide range of applications in civil, aeronautical, and offshore structures [1]. SHM technology uses discrete sensors mounted on or implanted in a host structure to enable continuous and real-time structural integrity assessment [2,3]. SHM systems can detect physical damage early on, allowing for on-demand repairs and maintenance. Therefore, smart structures facilitated with an SHM setup improve system reliability while lowering maintenance costs. Integrating prognosis into SHM strategies paves the way for condition-based maintenance [4,5].

Acousto-ultrasonic based SHM employs transient vibration feedback from the host structure at high-frequencies to determine the extent and location of the damage [6,7]. In structures made of thin plates, the elastic energy propagates in the form of Lamb waves, which are multi-modal and dispersive [8]. Some unique features of Lamb wave SHM include high sensitivity to incipient damage, damage localization, and the ability to inspect over a large area. Lamb wave SHM can be carried out in either pitch-catch or pulse-echo modes [9]. In the pitch-catch arrangement, the diagnostic signal emitted from an actuator passes through the damaged area while it is received by a sensor on the other side of the inspection area. In the pulse-echo scheme, the transducer acts as both an actuator and a sensor and captures the signal reflected by the damage. The selection of an appropriate layout for sensor-actuator pairs depends mainly on the type of the damage being inspected.

Modeling of ultrasonic guided wave propagation and its interaction with damage is of great importance in the process of system identification by Lamb waves [10,11]. Generation of dispersion curves [12], determination of wave-damage interaction coefficients [13], and optimal arrangement of transducer arrays are some of the Lamb wave modeling objectives. So far, a wide range of numerical methods have been employed to investigate the propagation of Lamb waves in thin-walled structures, including FEM [14-16], time-domain SFEM [17,18], frequency-domain SFEM [19], local interaction simulation approach [20], and the Boundary Element Method (BEM) [21]. Among them, FEM has been one of the most widely adopted methods due to its simple formulation and ability to handle complex geometries [20]. Nonetheless, using polynomial shape functions along with equidistant nodal points in FEM to capture the sinusoidal behavior of the waves dictates the mesh size reduction to at least 20 elements per the shortest wavelength of interest [22,23]. This rule of thumb, which leads to a very large number of Degrees of Freedom (DOFs) and overwhelming computational costs, especially in analyzing large domains, is the main drawback of FEM. This FEM deficiency is effectively overcome by implementing higher-order polynomial shape functions on non-equidistant nodal points in time-domain spectral methods [24]. Despite being more efficient than FEM, spectral methods require fine discretization for high-frequency regimes [25]. FEM and spectral methods are also suffering from a complex mesh generation process as they are not compatible with hanging nodes. This drawback complicates the study of typical SHM problems involving multi-material systems [20], stress singularities, and moving boundaries [26].

The Scaled Boundary Finite Element Method (SBFEM) is a semi-analytical approach to solving the governing partial differential equations of various systems more efficiently. Inspired by the fundamental ideas of FEM and BEM, SBFEM takes advantage of the strengths of both methods and overcomes their drawbacks [27]. More precisely, as in BEM, only the boundary of the analyzed domain needs to be discretized, thus reducing the dimensionality by one. There is no need to discretize the inside of the intended domain in SBFEM; this leads to a significant reduction in the required DOFs and the computational demands. Using an analytical solution in the radial direction enforces the radiation condition at infinity strictly [28]. However, unlike BEM, no fundamental solution is necessary. This feature classifies SBFEM as a semi-analytical method and makes it ideal to represent stress singularities at crack tips and notches [29]. SBFEM can be applied to uncoupled and coupled electro-mechanical [30] and thermo-mechanical [31] fields. The derived equations can be solved in either the time or frequency domain. SBFEM, which was originally developed by Song [32] for dynamic analysis of unbounded domains, has been successfully applied to a wide range of engineering areas such as elastostatics [33,34], inelasticity [35], elastodynamics [36-38], fracture mechanics [31,39-42], geotechnics [43], fluid mechanics [44], acousto-ultrasonics [25,45,46] and SHM [47-49].

In SBFEM, the process of discretizing the analyzed domain is simple and flexible. The possibility to discretize only the boundaries of the intended domain with elements of different sizes without any concern about hanging nodes facilitates mesh conformity establishment across non-homogeneous and discontinuous zones [50]. Recently, the development of polygon [51] and polyhedral Scaled boundary elements (S-elements) [52] for two and three dimensional SBFEM has enabled automatic mesh generation via quadtree [52] and octree [53] procedures. Furthermore, it is also possible to convert finite elements generated by any conventional FE mesh generator software package to S-elements [54,55]. The method handles automatic domain discretization and allows for the treatment of problems with complex geometries without the need for manual intervention.

Although SBFEM has been effectively implemented in a variety of engineering domains, it has not been employed for wafer PZT-based SHM approaches. Additionally, its three-dimensional implementation for the simulation of Lamb wave propagation and its experimental

validation have been rare. The purpose of this paper is to investigate the SBFEM's potential to simulate real-time Lamb wave health monitoring using PZT transducers. Modeling the PZT electromechanical effects enables direct output voltage comparison with experiments and more precise simulation of the sensor's actuation and sensing effects. To this end, an SBFEM formulation based on the equivalent load is proposed for simulation of Piezoelectric Wafer Active Sensors (PWAS) [56], often employed as sensor/actuator in SHM applications. Laboratory tests using the pitch-catch and pulse-echo techniques are used to validate the SBFEM results. The SBFEM's flexible meshing feature is used to model Lamb wave health monitoring of a stiffened plate. The computational efficiency of SBFEM is compared to FEM in terms of convergence rate, number of required DOFs, and computational time.

The paper is organized as follows. Section 2 summarizes the fundamental principles of the 3D SBFEM formulation for wave motion in homogeneous waveguides as well as the continued fraction solution procedure for bounded media. Section 3 deals with modeling the electromechanical effects of PWAS sensors in the context of SBFEM. The laboratory test setup is described in Section 4. The simulation details are presented in Section 5. Section 6 covers the implementation of the proposed approach for simulating Lamb wave propagation. Section 7 provides concluding remarks.

2. 3D SBFEM summary for elastodynamic problems

The 3D SBFEM equations for elastodynamic problems are briefly reviewed in this section. For a more extensive derivation and explanation of the method's basic concepts, see [57,58]. The use of continued fraction solution to analyze high-frequency wave motion problems is also highlighted [59].

In SBFEM, the governing equations are investigated in transformed scaled boundary coordinates. The scaling center criterion requires that the origin of this coordinate system O be positioned at a point from which the entire domain is directly visible. Fig. 1 shows the local radial (ξ) -circumferential (η, ζ) scaled boundary coordinates. ξ is defined on a line pointing to the boundary from the scaling center. In scaled boundary coordinates, each point's location is addressed by scaling a corresponding point on the boundary. The position of boundary points is obtained by interpolating the coordinates of the element nodes:

$$x(\xi,\eta,\zeta) = \xi\mathbf{N}(\eta,\zeta)\mathbf{x}; \quad y(\xi,\eta,\zeta) = \xi\mathbf{N}(\eta,\zeta)\mathbf{y}; \quad z(\xi,\eta,\zeta) = \xi\mathbf{N}(\eta,\zeta)\mathbf{z} \tag{1}$$

where $\mathbf{N}(\eta,\zeta)$ is the standard 2D FEM shape function constructed on the parent element in the circumferential coordinates, and $\boldsymbol{x}, \boldsymbol{y}$, and $\boldsymbol{z}$ are vectors of nodal coordinates. If the scaling requirement is met, the above transformation is unique. In scaled boundary coordinates, the frequency domain equations of motion in displacement are stated as follows for 3D problems [57]:

$$\mathbf{E}_0\xi^2\mathbf{u}(\xi)_{,\xi\xi} + \left(2\mathbf{E}_0 + \mathbf{E}_1^T - \mathbf{E}_1\right)\xi\boldsymbol{u}(\xi)_{,\xi} + \left(\mathbf{E}_1^T - \mathbf{E}_2\right)\mathbf{u}(\xi) + \mathscr{P}(\xi)$$
$$- \omega^2\mathbf{M}_0\xi^2\mathbf{u}(\xi)$$
$$= \mathbf{0} \tag{2}$$

where ω is the circular frequency, $\mathscr{P}(\xi)$ is the vector of equivalent nodal force functions consisting of external load contribution, and the coefficient matrices $\mathbf{E}_0, \mathbf{E}_1, \mathbf{E}_2$ and $\mathbf{M}_0$ are calculated as follows:

$$\mathbf{E}_0 = \sum_e \int_S \mathbf{B}_1^T(\eta,\zeta)\mathbf{CB}_1(\eta,\zeta)|\mathbf{J}_b| \; d\eta d\zeta$$

$$\mathbf{E}_1 = \sum_e \int_S \mathbf{B}_2^T(\eta,\zeta)\mathbf{CB}_1(\eta,\zeta)|\mathbf{J}_b| d\eta d\zeta$$

$$\mathbf{E}_2 = \sum_e \int_S \mathbf{B}_2^T(\eta,\zeta)\mathbf{CB}_2(\eta,\zeta)|\mathbf{J}_b| d\eta d\zeta \tag{3}$$

$$\mathbf{M}_0 = \sum_e \int_S \mathbf{N}^T(\eta,\zeta)\rho\mathbf{N}(\eta,\zeta)|\mathbf{J}_b| d\eta d\zeta$$
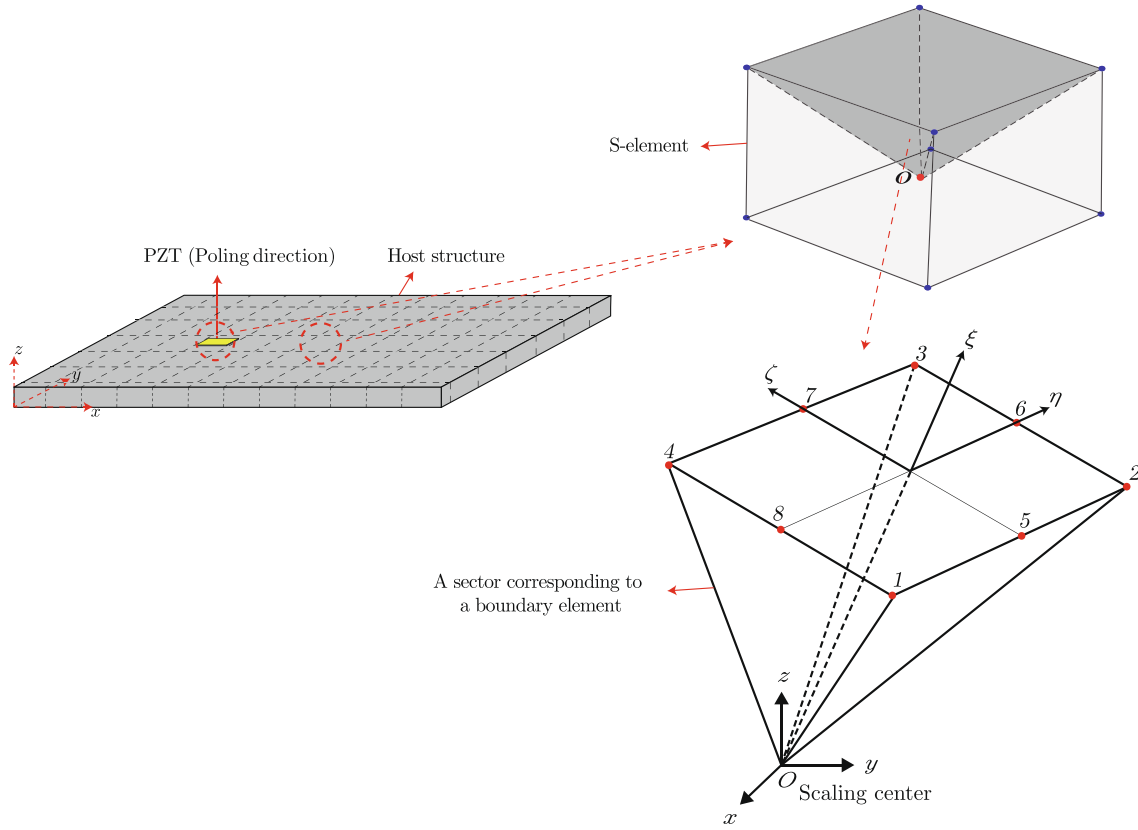
Fig. 1. Discretization of the solution domain using S-elements, and a partition of an S-element illustrated in local scaled boundary coordinates.

where $\mathbf{B}_1$ and $\mathbf{B}_2$ are strain-displacements matrices [55], $\mathbf{C}$ is the stiffness matrix, ρ is the mass density, $|\mathbf{J}_b|$ denotes the determinant of the Jacobian matrix of transformation from the Cartesian to the scaled boundary coordinates calculated on the boundary ($\xi = 1$), S denotes surface elements forming up an S-element, and $\sum_e$ stands for the standard FEM assembly procedure. By defining the dynamic stiffness matrix $\mathbf{S}(\omega, \xi)$ which relates the internal nodal force $\mathbf{q}(\xi)$ and nodal displacement $\mathbf{u}(\xi)$ as follows:

$$\mathbf{q}(\xi) = \mathbf{S}(\omega, \xi)\mathbf{u}(\xi) \tag{4}$$

and using the following relation for $\mathbf{q}(\xi)$ obtained by integrating the surface traction over the elements [57]:

$$\mathbf{q}(\xi) = \xi^2\left(\mathbf{E}_0\xi\mathbf{u}(\xi)_{,\xi} + \mathbf{E}_1^T\mathbf{u}(\xi)\right) \tag{5}$$

Eq. (2) can be expressed in terms of $\mathbf{S}(\omega, \xi)$ by eliminating $\mathbf{u}(\xi)$ and $\mathbf{q}(\xi)$ [59]:

$$(\mathbf{S}(\omega, \xi) - \mathbf{E}_1)\mathbf{E}_0^{-1}\left(\mathbf{S}(\omega, \xi) - \mathbf{E}_1^T\right) - \mathbf{E}_2 + \mathbf{S}(\omega, \xi) + \omega\mathbf{S}(\omega, \xi)_{,\omega} + \omega^2\mathbf{M}_0 = \mathbf{0} \tag{6}$$

which is evaluated on the boundary ($\xi = 1$) after replacing the partial differentiation relative to ξ with ω [59]. Because $\mathbf{S}(\omega, \xi)$ reflects inherent vibration charactereistics of an S-elemnt, $\mathscr{P}(\xi)$ is disregarded in derivation of Eq. (6).

Because there is no closed-form solution for Eq. (6), the solution procedure is case-dependent [60]. For high-frequency vibration, which is the focus of this study, $\mathbf{S}(\omega, \xi)$ can be solved using an improved continued fraction expansion up to order M_{cf} [59,61]:

$$\mathbf{S}(\omega, \xi) = \mathbf{K} - \omega^2\mathbf{M} - \omega^4\mathbf{X}^{(1)}\left(\mathbf{S}_0^{(1)} - \omega^2\mathbf{S}_1^{(1)} - \omega^4\mathbf{X}^{(2)}\left(\mathbf{S}_0^{(2)} - \omega^2\mathbf{S}_1^{(2)} - \ldots \right.\right.$$
$$\left.\left. - \omega^4\mathbf{X}^{(M_{cf})}\left(\mathbf{S}_0^{(M_{cf})} - \omega^2\mathbf{S}_1^{(M_{cf})}\right)^{-1}\left(\mathbf{X}^{(M_{cf})}\right)^T\right)^{-1}\ldots\left(\mathbf{X}^{(2)}\right)^T\right)^{-1}\left(\mathbf{X}^{(1)}\right)^T \tag{7}$$

$\mathbf{K}$ and $\mathbf{M}$ are the static stiffness and mass matrices, $\mathbf{S}_0^{(i)}$ and $\mathbf{S}_1^{(i)}$ ($i = 1, 2, \ldots, M_{cf}$) can be considered the contribution of high-frequency modes to the stiffness and mass matrices [37]. These matrices are computed recursively by substituting Eq. (7) into Eq. (6), arranging them in an ascending order of powers of ω^2, and setting the coefficients equal to zero [61]. Scaling factor matrices $\mathbf{X}^{(i)}$ in Eq. (7) are introduced to prevent large condition numbers for structural matrices in large-scale problems [62]. The continued fraction expansion of the dynamic stiffness results in a set of linear equations that can be collected in the matrix form below:

$$\mathbf{K}_h\mathbf{z}(\omega) - \omega^2\mathbf{M}_h\mathbf{z}(\omega) = \mathbf{F}(\omega) \tag{8}$$

$$\mathbf{K}_h = \text{diag}\left(\mathbf{K}, \mathbf{S}_0^{(1)}, \mathbf{S}_0^{(2)}, \ldots, \mathbf{S}_0^{(M_{cf})}\right) \tag{9}$$

$$\mathbf{M}_h = \begin{bmatrix} \mathbf{M} & -\mathbf{X}^{(1)} & \mathbf{0} & \cdots & \mathbf{0} & \mathbf{0} \\ -\left(\mathbf{X}^{(1)}\right)^T & \mathbf{S}_1^{(1)} & -\mathbf{X}^{(2)} & \cdots & \mathbf{0} & \mathbf{0} \\ \mathbf{0} & -\left(\mathbf{X}^{(2)}\right)^T & \mathbf{S}_1^{(2)} & \cdots & \mathbf{0} & \mathbf{0} \\ \vdots & \vdots & \vdots & \ddots & \vdots & \vdots \\ \mathbf{0} & \mathbf{0} & \mathbf{0} & \cdots & \mathbf{S}_1^{(M_{cf-1})} & -\mathbf{X}^{(M_{cf})} \\ \mathbf{0} & \mathbf{0} & \mathbf{0} & \cdots & -\left(\mathbf{X}^{(M_{cf})}\right)^T & \mathbf{S}_1^{(M_{cf})} \end{bmatrix} \tag{10}$$

$$\mathbf{z}(\omega) = \left\{ \mathbf{u}(\omega) \quad \mathbf{u}^1(\omega) \quad \mathbf{u}^2(\omega) \quad \cdots \quad \mathbf{u}^{(M_{cf}-1)}(\omega) \quad \mathbf{u}^{(M_{cf})}(\omega) \right\}^T \tag{11}$$

$$\mathbf{F}(\omega) = \left\{ \mathbf{R}(\omega) \quad \mathbf{0} \quad \mathbf{0} \quad \cdots \quad \mathbf{0} \quad \mathbf{0} \right\}^T \tag{12}$$

The $\mathbf{R}(\omega)$ and $\mathbf{u}(\omega)$ vectors denote nodal loads and displacements at the discretized boundary. The $\mathbf{u}^i(\omega)$, $(i = 1, \ldots, M_{cf})$ vectors are auxiliary variables that relate to the higher-order stiffness terms and have no physical meaning. The global structural matrices are formed using the conventional FEM assembly procedure on S-element matrices. After adding damping, the equations of motion in the frequency domain are read as follows:

$$\mathbf{K}_G \mathbf{z}_G(\omega) + i\omega \mathbf{C}_G \mathbf{z}_G(\omega) - \omega^2 \mathbf{M}_G \mathbf{z}_G(\omega) = \mathbf{F}_G(\omega) \tag{13}$$

where the subscript G refers to global matrices. The time-domain equation of motion is obtained by applying an inverse Fourier transform to Eq. (13):

$$\mathbf{K}_G \mathbf{z}_G(t) + \mathbf{C}_G \dot{\mathbf{z}}_G(\omega) + \mathbf{M}_G \ddot{\mathbf{z}}_G(t) = \mathbf{F}_G(t) \tag{14}$$

which is a typical form of the structural dynamic equation that can be solved using direct time-integration algorithms.

3. SBFEM-based PWAS modelling

An effective method for modeling the actuation and sensing effects of PWAS frequently used in real-time SHM approaches is proposed in the context of SBFEM. The idea is to model the electromechanical coupling effect of PWAS as an equivalent body load rather than employing electrical DOFs for its nodes [29,30,36,63,64]. This approach reduces PWAS DOFs while maintaining sufficient accuracy for extremely thin PZTs used in SHM [16]. Assuming that body loads have negligible effect on shape functions, their contribution to SBFEM equations can be dealt with in the virtual work balance rather than the analytical part [65]. The following is the virtual work of body loads in an S-element of the PZT material:

$$\delta U_b = \delta \mathbf{d}^T \mathbf{R}_b \tag{15}$$

where $\mathbf{R}_b$ is the equivalent nodal body load and $\mathbf{d}$ is the extracted displacements from the global physical DOF vector ($\mathbf{u}(t)$ in the first block of $\mathbf{z}(t)$ in Eq. (14)) that match the intended S-element. In order to find $\mathbf{R}_b$, the virtual electromechanical work of the PZT is examined. Consider the following stress-charge form of standard linear piezoelectric constitutive equations [29]:

$$\boldsymbol{\sigma} = \mathbf{C}^E \boldsymbol{\varepsilon} - \mathbf{e}^T \mathbf{E} \tag{16}$$

$$\mathbf{D} = \mathbf{e}\boldsymbol{\varepsilon} + \boldsymbol{\epsilon}^\varepsilon \mathbf{E} \tag{17}$$

where $\boldsymbol{\sigma}$ and $\boldsymbol{\varepsilon}$ denote the stress and strain vectors, $\mathbf{D}$ the electric displacement, $\mathbf{E}$ the electric field vector, $\mathbf{C}^E$ the stiffness matrix, $\mathbf{e}$ the electromechanical coupling coefficient matrix, and $\boldsymbol{\epsilon}^\varepsilon$ the permittivity matrix. Superscripts E and ε indicate values at constant electric field and constant strain, respectively. In the absence of mechanical point, surface, and body loads, as well as electric point, and body charges, the virtual work of the PZT is as follows [66]:

$$\int_{V^e} \delta \boldsymbol{\varepsilon}^T \mathbf{C}^E \boldsymbol{\varepsilon} dV + \int_{V^e} \delta \mathbf{u}^T \rho \ddot{\mathbf{u}} dV = \int_{V^e} \delta \boldsymbol{\varepsilon}^T \mathbf{e}^T \mathbf{E} dV \tag{18}$$

$$\int_{V^e} \delta \mathbf{E}^T \mathbf{e}\boldsymbol{\varepsilon} dV + \int_{V^e} \delta \mathbf{E}^T \boldsymbol{\epsilon}^\varepsilon \mathbf{E} dV = \int_{A_\varphi} \delta \varphi q_s dA \tag{19}$$

where φ denotes the potential, q_s the applied surface charge density, V^e the volume of a sector of the S-element, and A_q that part of the boundary where charge is prescribed. For ease of notation, the superscript e indicating a boundary element of an S-element is eliminated for integral

expressions and only remains for their bounds (V^e). Fully coupled electromechanical treatment of the PWAS requires simultaneous analysis of Eq. (18) and Eq. (19). Nonetheless, because of the PWAS's low thickness and unobtrusive nature, some simplifying assumptions can be made, allowing for a more efficient one-way coupling analysis scheme. For the actuator PZT, the electric field/charge induced by the host structure vibration is negligible compared to the strain induced by electric actuation and thus can be ignored. Hence, Eq. (19), which reflects the sensing property of the actuator PWAS, can be disregarded. The left side of Eq. (18) is the same as for the host structure, and it leads to stiffness and mass matrices for the PWAS element, which are inserted into the left side of Eq. (14) during the assembly process. The right-side term refers to the virtual electromechanical energy delivered by the PWAS to the host structure δU_{em}^e. To compute δU_{em}^e, the strain at any point in the S-element's sector is recovered from nodal displacements as follows [57]:

$$\boldsymbol{\varepsilon} = \boldsymbol{\Psi}_b^{(\varepsilon)e} \xi^{\mathbf{S}_b - 1.5\mathbf{I}} \left(\boldsymbol{\Psi}_b^{(u)} \right)^{-1} \mathbf{d} \tag{20}$$

where $\boldsymbol{\Psi}_b^{(u)}$ and $\mathbf{S}_b$ are derived from the solution of the analytical part of the SBFEM [57,58]. The superscript u in $\boldsymbol{\Psi}_b^{(u)}$ indicates a partition of $\boldsymbol{\Psi}_b$ associated with the displacement solution. The superscript e indicates the displacement modes corresponding to the intended element's DoFs obtained by extracting the corresponding rows of $\boldsymbol{\Psi}_b^{(u)}$. In Eq. (20), $\boldsymbol{\Psi}_b^{(\varepsilon)}$ represents the strain modes, which are made up of displacement modes as follows:

$$\boldsymbol{\Psi}_b^{(\varepsilon)e} = \left(\mathbf{B}_1(\eta, \zeta) \boldsymbol{\Psi}_b^{(u)e} (\mathbf{S}_b - 0.5\mathbf{I}) + \mathbf{B}_2(\eta, \zeta) \boldsymbol{\Psi}_b^{(u)e} \right) \tag{21}$$

By inserting Eq. (20) into the δU_{em}^e definition on the right side of Eq. (18), we get:

$$\delta U_{em}^e = (\delta \mathbf{d})^T \int_{V^e} \left(\boldsymbol{\Psi}_b^{(u)} \right)^{-T} \xi^{\mathbf{S}_b^T - 1.5\mathbf{I}} \left(\boldsymbol{\Psi}_b^{(\varepsilon)e} \right)^T \mathbf{e}^T \mathbf{E} dV \tag{22}$$

Adding up the contributions of each element δU_{em}^e yields the virtual electromechanical energy in the S-element δU_{em}:

$$\delta U_{em} = \sum_e \delta U_{em}^e = \delta \mathbf{d}^T \sum_e \int_{V^e} \left(\boldsymbol{\Psi}_b^{(u)} \right)^{-T} \xi^{\mathbf{S}_b^T - 1.5\mathbf{I}} \left(\boldsymbol{\Psi}_b^{(\varepsilon)e} \right)^T \mathbf{e}^T \mathbf{E} dV \tag{23}$$

By comparing Eq. (23) with Eq. (15), the nodal load equivalent to the electromechanical actuation of the PWAS is derived as follows:

$$\mathbf{R}_b = \sum_e \int_{V^e} \left(\boldsymbol{\Psi}_b^{(u)} \right)^{-T} \xi^{\mathbf{S}_b^T - 1.5\mathbf{I}} \left(\boldsymbol{\Psi}_b^{(\varepsilon)e} \right)^T \mathbf{e}^T \mathbf{E} dV \tag{24}$$

The above integration can be carried out analytically in the radial direction. The volume integral is separated into the integrals in radial and circumferential direction and dV is replaced with $\xi^2 |\mathbf{J}_b| \, d\xi dS$:

$$\mathbf{R}_b = \sum_e \int_0^1 \int_S \left(\boldsymbol{\Psi}_b^{(u)} \right)^{-T} \xi^{\mathbf{S}_b^T - 1.5\mathbf{I}} \left(\boldsymbol{\Psi}_b^{(\varepsilon)e} \right)^T \mathbf{e}^T \mathbf{E} \xi^2 |\mathbf{J}_b| \, d\xi dS \tag{25}$$

Considering the electric field is uniform over the thin PZT, $\mathbf{R}_b$ can be rewritten as follws:

$$\mathbf{R}_b = \left(\boldsymbol{\Psi}_b^{(u)} \right)^{-T} \int_0^1 \xi^{\mathbf{S}_b^T + 0.5\mathbf{I}} \left(\sum_e \int_S \left(\boldsymbol{\Psi}_b^{(\varepsilon)e} \right)^T |\mathbf{J}_b| \, dS \right) d\xi \mathbf{e}^T \mathbf{E} \tag{26}$$

The integral in the circumferential direction is not a function of ξ and is represneted as $\mathbf{R}_{b_0}$ after assembling over boundary elements:

$$\mathbf{R}_{b_0} = \sum_e \int_S \left(\boldsymbol{\Psi}_b^{(\varepsilon)e} \right)^T |\mathbf{J}_b| \, dS \tag{27}$$

Using Eq. (27), $\mathbf{R}_b$ is read as follows:

$$\mathbf{R}_b = \left(\boldsymbol{\Psi}_b^{(u)} \right)^{-T} \left(\int_0^1 \xi^{\mathbf{S}_b^T + 0.5\mathbf{I}} d\xi \right) \mathbf{R}_{b_0} \mathbf{e}^T \mathbf{E} \tag{28}$$

Integrating in the radial direction analytically results in $\mathbf{R}_b$ as follows:

$$\mathbf{R}_b = \left(\boldsymbol{\Psi}_b^{(u)}\right)^{-T}(\mathbf{S}_b^T + 1.5\mathbf{I})^{-1}\mathbf{R}_{b_0}\mathbf{e}^T\mathbf{E} \qquad (29)$$

In Lamb wave health monitoring, a voltage V_a in the form of a tone-burst between the top and bottom surface electrodes actuates the PWAS. It generates a uniform electric field in the polarization direction, which is supposed to be parallel to the z-axis, as follows [67]:

$$\mathbf{E} = \frac{1}{h}[0 \ \ 0 \ \ 1]^T V_a = \mathbf{h}V_a \qquad (30)$$

where h is the PZT thickness. The explicit expression of the PWAS electromechanical actuation force given as an equivalent mechanical load is obtained by replacing $\mathbf{E}$ in Eq. (28) with Eq. (30):

$$\mathbf{R}_b = \left(\boldsymbol{\Psi}_b^{(u)}\right)^{-T}(\mathbf{S}_b + 1.5\mathbf{I})^{-1}\mathbf{R}_{b_0}\mathbf{e}^T\mathbf{h}V_a \qquad (31)$$

Eq. (31) is integrated into the right side of the global equations, i.e., Eq. (14). In Lamb wave experiments, PWAS actuation is the only input to the system in the absence of any other external mechanical or electrical loads, which means that $\mathbf{R}$ in Eq. (12) is only the $\mathbf{R}_b$ in Eq (31).

For the sensory PWAS, on the other hand, Eq. (18), which describes the PZT influence on the host structure vibration, can be ignored. Solving Eq. (19) with q_s set to zero yields the electric field in the sensory PWAS, which can then be converted to electric potential using Eq. (30). In an equivalent approach, the electric charge may be computed using Gauss's law in terms of electric displacement field as follows:

$$Q = \int_A \mathbf{D}^T d\mathbf{A} \qquad (32)$$

where $d\mathbf{A}$ is the normal vector to the PWAS surface and Q is the PWAS charge, and A is either the top or bottom surface of the PZT. In the above equation, the electric displacement $\mathbf{D}$ is obtained from Eq. (17) after solving for the displacements $\mathbf{d}$ and recovering strains ε at Gauss points of the surface elements on the top/bottom of the PWAS S-elements. The electric field in Eq. (17) is replaced by Eq. (30) where the actuation voltage V_a is set equal to the actuation voltage applied to the PWAS in the pulse-echo and zero in the pitch-catch arrangements. Having PWAS charge, the sensor voltage is obtained from the capacitance C_p of the PWAS:

$$V_s(t) = \frac{Q(t)}{C_p} = \frac{Q(t)h}{\epsilon_z^\varepsilon A} \qquad (33)$$

where ϵ_z^ε is the thickness-direction permittivity component, A is the PWAS top/bottom surface area.

To summarize, the Lamb wave SHM can be simulated using SBFEM employing a uniform distribution for the electric potential over the thickness of the PWAS and a one-way electromechanical coupling of the PWAS with the host structure, as shown in Fig. 2.

4. Experimental setup

The Lamb wave experiments in pitch-catch arrangement were conducted on a 2 mm thick plate. The pulse-echo experiments were performed on a 1 mm thick plate with a notch that was cut using electrical discharge machining (Fig. 3). The PWAS (PZT 5H) sensors, each with a thickness of 0.267 mm, were mounted on the plates using a two-part epoxy. The bottom surface of the PWAS was accessed using conductive copper tape. The specimen was supported by packing foam during the experiment to approximate the free boundary condition. The actuation signal was transmitted to the PWAS through the Agilent 33220A function generator. The PWAS voltage was recorded using a PicoScope 4424 oscilloscope at an 80 MS/s sampling rate.

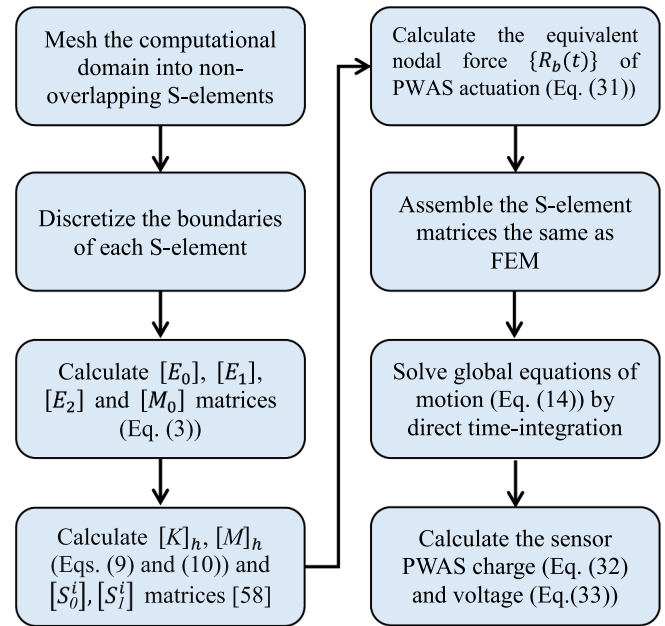The actuation signal is a 5-count Hanning-windowed tone-burst (see

Fig. 2. SBFEM for simulation of PWAS-based Lamb wave health monitoring.

Fig. 4) applied to the top surface of the PZT while the bottom surface is grounded. In the pulse-echo method, the amplitude of the sensed signal is small compared to the actuation signal. Thus, the actuated signal is often clipped to improve the resolution of the reflected wave packets and make them visible and recognizable.

5. Numerical simulation

Lamb wave propagation in thin plates, identical to that utilized in the experimental tests (Fig. 3), was simulated using SBFEM and FEM. Table 1 lists the material properties of the aluminum and PZT 5H used in simulations, with the latter data taken from the PZT datasheet.

To provide the initial discretization, the SBFEM discretization module can be connected to any conventional FE generator. The module converts a standard finite element into an S-element, which is merely discretized at the boundaries. The transformation of a 20-node hexahedron into a 20-node S-element with quadratic surface elements (Q8) at the boundaries is illustrated in Fig. 5. Each S-element is stored as an array of boundary faces (s_1 to s_6 in Fig. 5). The faces are stored via their constituent nodes in an order that results in an outward normal to the face. It should be noticed that the quality of the original imported discretization affects the quality of the S-elements. However, the S-elements are more resistant to distortion and high aspect ratios because they are only discretized at the boundary. For instance, a warped 3D FE with high aspect ratios can be converted into an S-element with high-quality surface elements at the boundary.

To be able to compare the computing costs of SBFEM with FEM, the ABAQUS (version R2019x) structural matrices import tool was employed. The structural matrices generated through the analytical solution in the radial direction in SBFEM by MATLAB (version R2019b) are imported into ABAQUS. Time integration was carried out using the Hilber-Hughes-Taylor method with alpha, beta, and gamma values of −0.05, 0.27, and 0.55, respectively. The minimum time-increment was deemed to be 0.1 microseconds for a smooth output signal. Electric signals are applied to the top face of the PZT as inputs, such as a 10 V peak-to-peak, five-cycle tone-burst with a pre-set centre frequency. In SBFEM, Eq. (31) transforms electric actuation signals into mechanical equivalent loads. In FEM, however, the electrical DOF is taken into account for the PWAS elements, and the electrical boundary conditions were applied directly to the PWAS nodes. As in the experimental test,
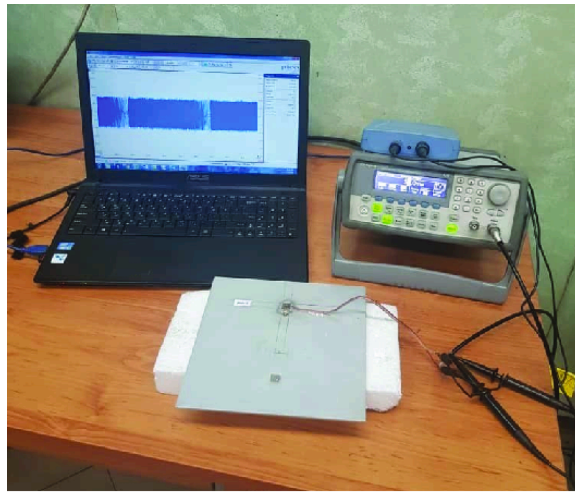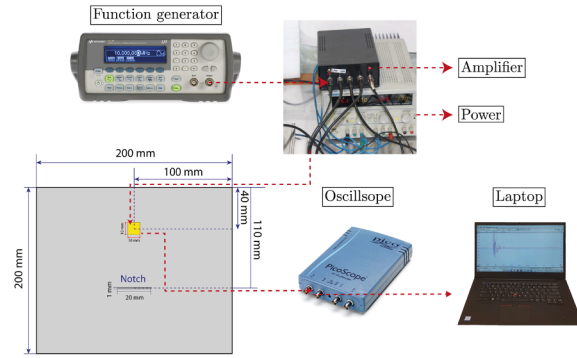
(a)   (b)

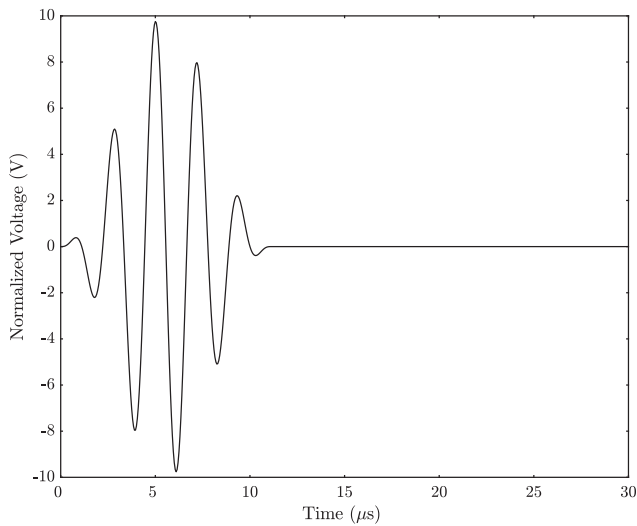**Fig. 3.** Lamb wave health monitoring experimental setup.

Fig. 4. Actuation signal used in the Lamb wave test of the notched plate: zero padded 5-cycle tone-burst with 450 kHz central frequency.

Table 1
Mechanical and electrical properties of Al and PZT 5H.

Property	Symbol	Al	PZT-5H	Units
Young modulus	E	71	62	GPa
Poisson ratio	ν	0.33	0.31	–
Density	ρ	2750	7870	$\frac{kg}{m^3}$
Rayleigh damping coefficients	α	10^{-3}	10^{-3}	s^{-1}
	β	8×10^{-8}	8×10^{-8}	s
Relative permittivity	$\epsilon_{11}^{\varepsilon} = \epsilon_{22}^{\varepsilon}$	–	3130	–
	$\epsilon_{33}^{\varepsilon}$		3400	
Piezoelectric constants	$e_{13}^{T} = e_{23}^{T}$	–	−6.5	$\frac{C}{m^2}$
	e_{33}^{T}	–	23.3	$\frac{C}{m^2}$
	$e_{15}^{T} = e_{24}^{T}$	–	17.44	$\frac{C}{m^2}$

free mechanical boundary condition was considered for the models. The longest radial distance of the S-elements determines the order of the continued fraction expansion M_{cf} [37]. The mesh size of SBFEM and FEM is adjusted based on a convergence study that is discussed in more detail below.

5.1. Convergence study

Convergence analysis was performed in both h-refinement and p-refinement strategies to estimate the mesh size for the SBFEM and FEM models. To achieve h-refinement in the SBFEM context, the number of S-elements or the number of individual boundary elements connected to S-elements might be increased. Here, the former scheme was adopted for h-refinement. The eigen-frequency of the system is calculated by solving the eigenvalue problem associated with Eq. (13), ignoring the damping term. The average of the absolute relative differences between the first N eigen-frequencies of the current model and a potentially converged model is used as an error estimator [48]:

$$\bar{\varepsilon} = \frac{1}{N} \sum_{i=1}^{N} \left| \frac{f_i - F_i}{F_i} \right| \tag{34}$$

where f_i and F_i are the ith eigen-frequencies of the current discretization and a model with a very fine mesh size, respectively. N is adjusted to include the relevant frequency range. In the stiffened plate case, for instance, N is set at 310 to cover the frequency range up to more than 200 kHz, which is the actuation's central frequency. Fig. 6 shows the mean absolute relative error $\bar{\varepsilon}$ versus total DOFs in logarithmic scale for successive mesh size reduction steps. The electrical DOFs are also taken into account for FEM. Fig. 6 is used to calculate the required number of DOF or the associated mesh dimension for a given percentage of error. According to the figure, SBFEM with linear boundary elements requires approximately 4 times less DOFs than FEM for a given error. The DOF reduction ratio for SBFEM with quadratic boundary elements relative to FEM is more than 8 times. This amount of DOF reduction leads to significant computing time reduction in time domain analysis which is given in Table 2 for the examined examples.

To examine the convergence rate, a linear relation in the logarithmic scale is fitted to the convergence data; see Fig. 6. The slopes of the fit, i.e., the exponent of the fit in the linear scale, show that SBFEM has a substantially faster convergence rate than FEM. This is due to SBFEM's use of an analytical solution in one direction, which reduces the discretization dimension by one. The presence of an analytical solution along the radial direction in SBFEM avoids the requirement for mesh refinement around the notch, hence the rate of convergence is unaffected. Furthermore, reducing the DOF results in fewer machine
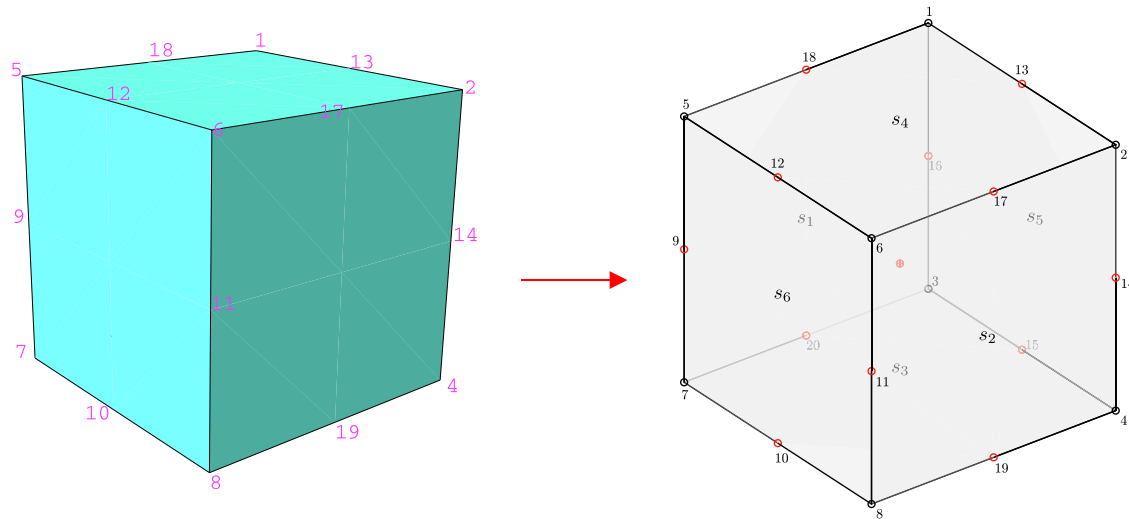
Fig. 5. The conversion of a 20-node quadratic hexahedron FE (left) into a 20-node S-element with Q8 boundary elements (right).
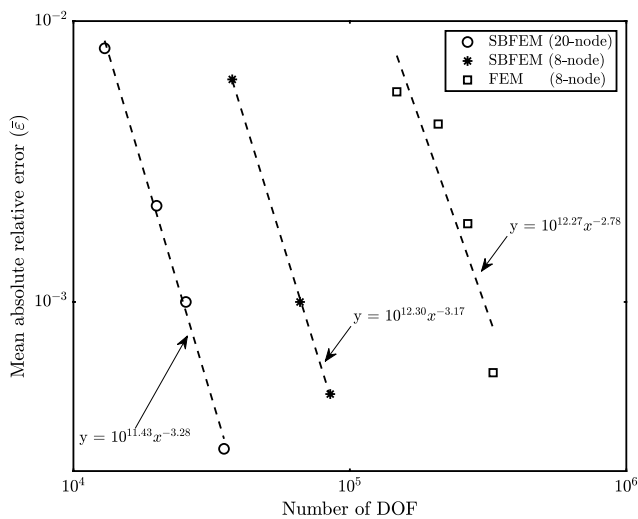

Fig. 6. Convergence analysis results for SBFEM and FEM simulation of the stiffened plate.

computations and, thus, fewer round-off errors in SBFEM. Fig. 6 further indicates that quadratic boundary elements associated with 20-node S-elements have a faster rate of convergence than linear boundary elements associated with 8-node S-elements.

6. Results and discussion

The numerical results of the SBFEM simulation of Lamb wave health monitoring are presented in this section. To evaluate the SBFEM performance, the results are compared to their experimental and FEM counterparts. The case studies include the Lamb wave propagation in a pristine plate, a cracked plate, a notched plate, and a stiffened plate.

6.1. Lamb wave propagation in the pitch-catch scheme

In the pitch-catch setup for the sensors, the Lamb wave propagation for a 1 mm thick aluminum plate was investigated. The schematic of the plate and the PWASs, along with their dimensions, are shown in Fig. 7 (a). By adjusting the spacing between the PWASs $2a$ to 10 mm, a free space is preserved between the direct wave and the boundary reflected packets in the sensory signal for the damage packet.

In order to prevent the detected signal from being corrupted by the plate boundary reflected waves, the actuation signal was also tuned with the PWAS to minimize the A0 mode actuation [68]. The tuning curve for the plate and the 7 mm PWAS is shown in Fig. 8. The figure shows that when the actuator PWAS is excited with central frequency f_c of 270 kHz, the S0 mode becomes overwhelming. As a result, there would be less confluence between the direct transmitted A0 and the damage reflected S0, the latter of which is about 2.7 times faster according to the dispersion curve.

The crack is modeled as a seam having duplicated nodes which lead to crack opening in the wave traversing term. The S-elements and their scaling centers that were used to discretize the cracked plate are depicted in Fig. 9. The actuator PWAS is subjected to a 5-cycle tone burst with a frequency of 270 kHz as the actuation signal, and Eq. (31) is used to convert it into the body load.

Fig. 10 shows the sensor signal of the experiment and SBFEM simulation. The great conformity between the results indicate the validity of the provided formulation. Owing to the actuation tuning, the A0 is almost absent in the direct sensed signal and there is more than 45 μs free space to collect the damage reflected signal.

The experimental and SBFEM-simulated sensor signals for the cracked plate are shown in Fig. 11. The damage reflected S0 mode reaches the sensor 34 μs after the direct wave packet in the free space between wave packets. The damage reflected wave's time of flight is 34 μs, which is consistent with the location of the crack, i.e., x_c of 90 mm and y_c of 7 mm. Strong agreement between the data shows that SBFEM can precisely mimic the lamb wave health monitoring.
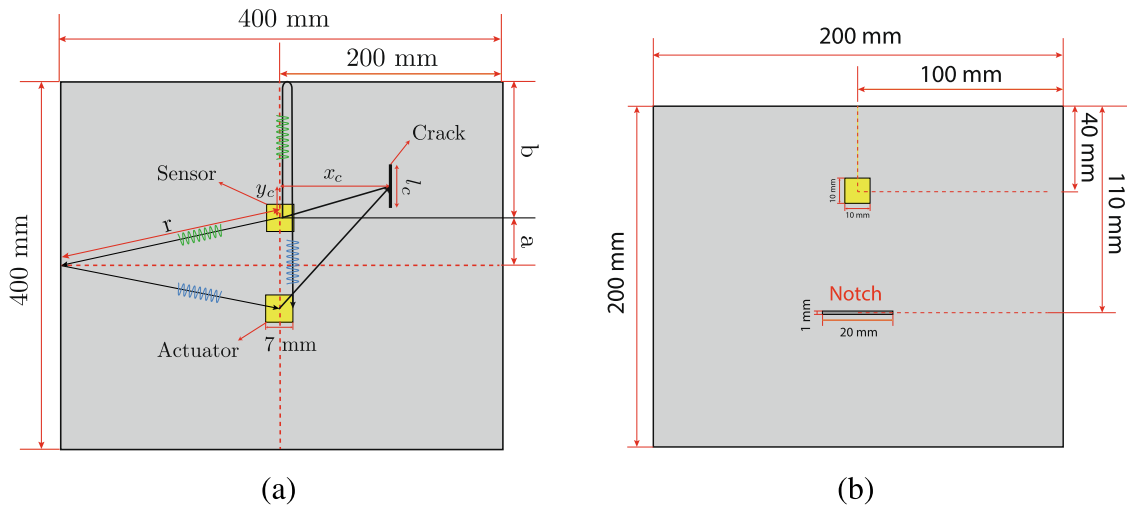
Table 2

Comparison of the SBFEM and FEM simulations; simulation time increment is 0.1 μs.

Simulation time	Notched plate example 32 μs			Stiffened plate example 200 μs		
	FEM (8 node)	SBFEM (8 node)	SBFEM (20 node)	FEM (8 node)	SBFEM (8 node)	SBFEM (20 node)
Number of DoFs	311,032	66,020	25,510	1,747,786	436,947	218,473
CPU time (min)	29.8	6.3	2.6	366.5	89.7	44.9

Fig. 7. Schematic of the plates instrumented with PWAS: (a) 2 mm thick cracked plate used in pitch-catch tests, (b) 1 mm thick notched plate used in pulse-echo tests.
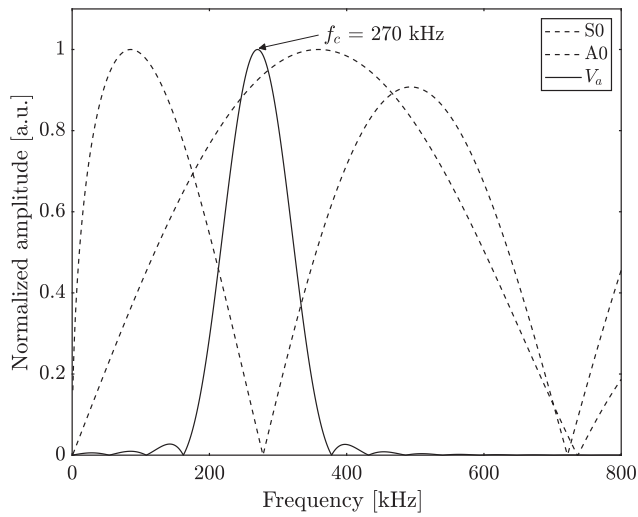

Fig. 8. Lamb wave response of a 2 mm thick plate tuned by 7 mm PWAS excitation.

6.2. Lamb wave propagation in the pulse-echo scheme

Fig. 12 depicts the SBFEM and FEM discretization of the notched plate. To evaluate the benefits of p-refinement, the boundaries of the S-elements are discretized in SBFEM using 4-node linear (Q4) and 8-node quadratic (Q8) surface elements. The FE model was discretized using 8-node linear solid elements. The model's discontinuous regions are the interfaces between the defect and the PWAS with the host structure. The mesh size is reduced around the discontinuities in FEM, and it gradually becomes coarser a bit more. In SBFEM, mesh refining is eliminated when the scaling centre for S-elements associated with discontinuities is properly selected. The location of the scaling centres on the interface-aligned surface elements is shown in Fig. 12.

The time-domain equation (Eq. (14)) was integrated to investigate the pulse-echo propagation of the Lamb wave in the notched plate.
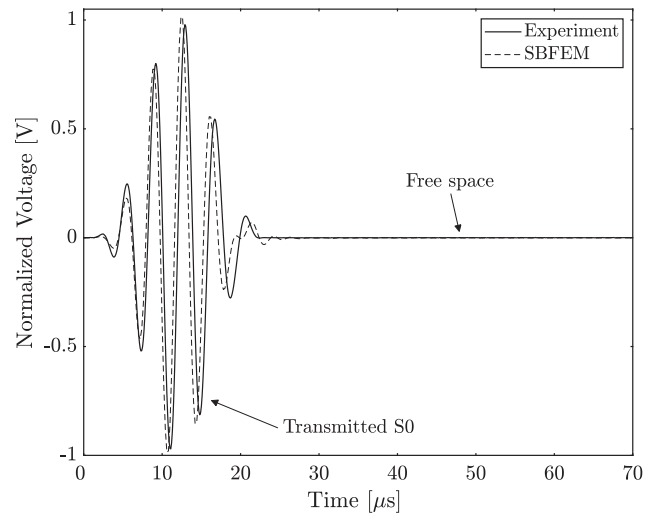

Fig. 10. The sensor PWAS voltage in the pitch-catch test of the pristine plate.
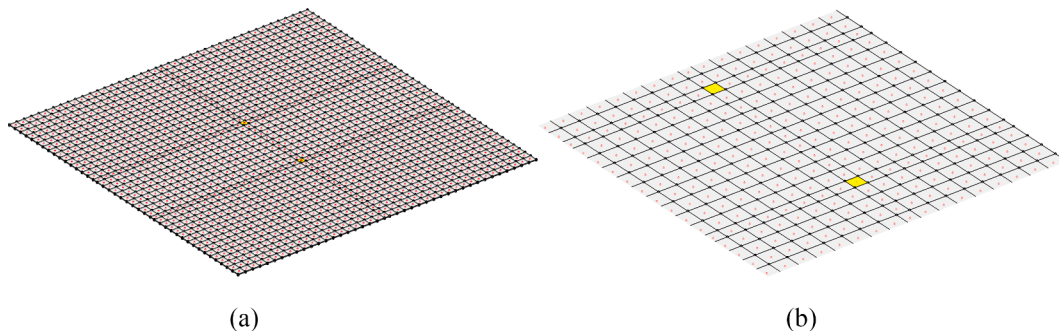

Fig. 9. (a) SBFEM discretization of the cracked plate instrumented with two PWASs for pitch-catch experiments (b) magnified view around the sensors.
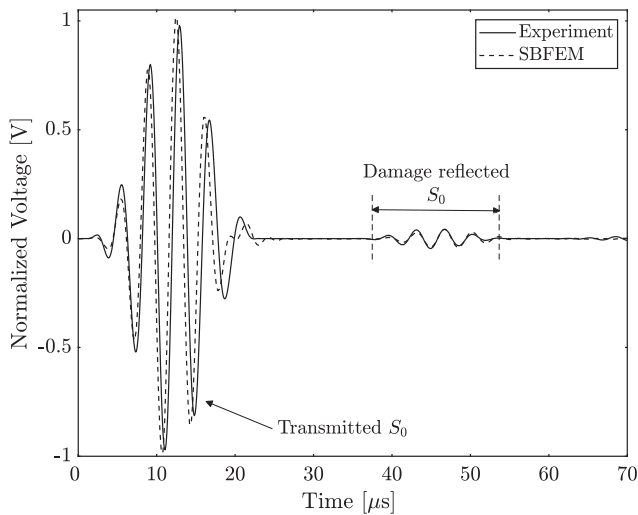
Fig. 11. The sensor PWAS voltage in the pitch-catch test of the cracked plate.

Fig. 13 depicts the voltage of the PWAS for 32 μs. As explained previously, in the pulse-echo technique, the initial packet of the signal that rides on the actuation signal is clipped to increase the resolution of the bounced-back waves. This segment of the signal contains no information about damage or system characteristics. In the numerical model, the actuator and sensor PZTs were separated from each other using the trick of halving the PWAS patch. The graphs depicted in Fig. 13 concern the voltage of the sensor half of the PWAS. In this way, the actuation signal does not ride on the sensed signal, and that is why the first portion of the numerical results is within the range of the reflected-back packets. The remainder of the signal in Fig. 13 represents the symmetric S0 and antisymmetric A0 modes of the edge reflected wave. The agreement between the SBFEM and experimental results validates the proposed formulation. The slight discrepancy in the results is partially due to the edge effect and its consequences on the reflected wave, such as wave dissipation or mode conversion. In practice, the structure's edges are not as flawlessly smooth as the computational simulations suggest. Hence, the numerical model does not account for the impact of edge roughness on the reflected wave. Uncertainty in the host structure and PWAS material properties is another factor contributing to the differences between the model and test results.

The FEM results are also computed to the same accuracy as SBFEM and are rendered for comparison in Fig. 13. The number of DOFs and the CPU times of the SBFEM are compared with those of FEM in Table 2. The

simulations are performed on a desktop PC (AMD Ryzen 7 1700 8-core CPU, 3 GHz, 16 GB RAM). In terms of the required computational time, SBFEM requires more preprocessing CPU time than FEM. The solution time, however, is several orders of magnitudes shorter than FEM, and the difference is more noticeable when used to simulate a longer propagation duration as shown in the next example.

6.3. Lamb wave health monitoring of a stiffened plate

Fig. 14 shows the discretization of the plate with stiffener and two mounted PWASs in SBFEM and FEM. The thicknesses of the stiffener and plate are 0.8 and 1 mm, respectively. The PZTs are $10 \times 10 \times 0.267$ mm³ in size. The actuation signal is a 5-count smoothed tone-burst with a central frequency of 200 kHz (Fig. 4) that was applied to the left PWAS in Fig. 14.

The voltage of the sensor PWAS is depicted in Fig. 15. The waveform is more complex than the previous models due to the stiffener influence on the wave. However, the symmetric and antisymmetric packets of the sensed wave can still be distinguished. Moreover, the received signal contains some mixed modes due to mode conversion and dispersion.

The remarkable agreement between the SBFEM and convergent FEM data reveals that the former's formulation and implementation are valid.
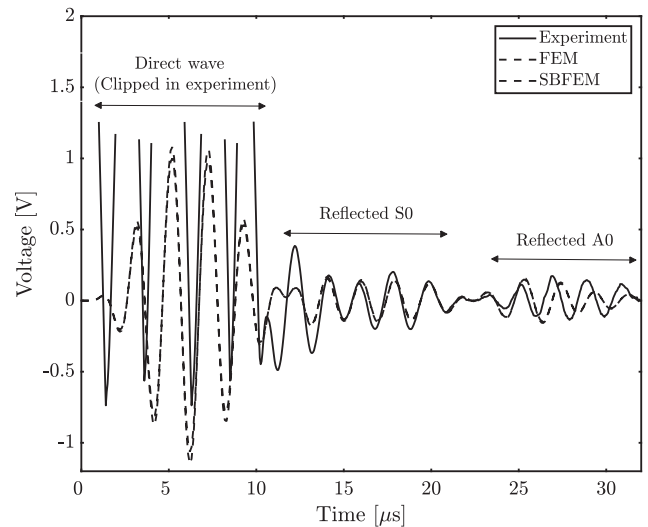

Fig. 13. Experimental and numerical (FEM and SBFEM) results of the PWAS voltage installed on the notched plate in the pulse-echo tests.
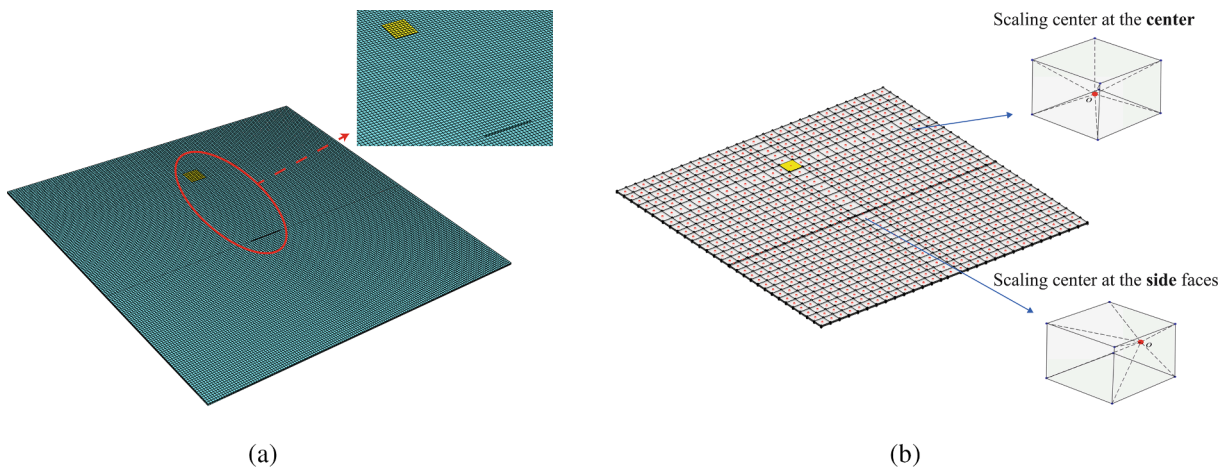

| (a) | (b) |

Fig. 12. Discretization of the notched plate instrumented with PWAS for (a) FEM, and (b) SBFEM simulations; the red dots show the scaling center positions. (For interpretation of the references to colour in this figure legend, the reader is referred to the web version of this article.)
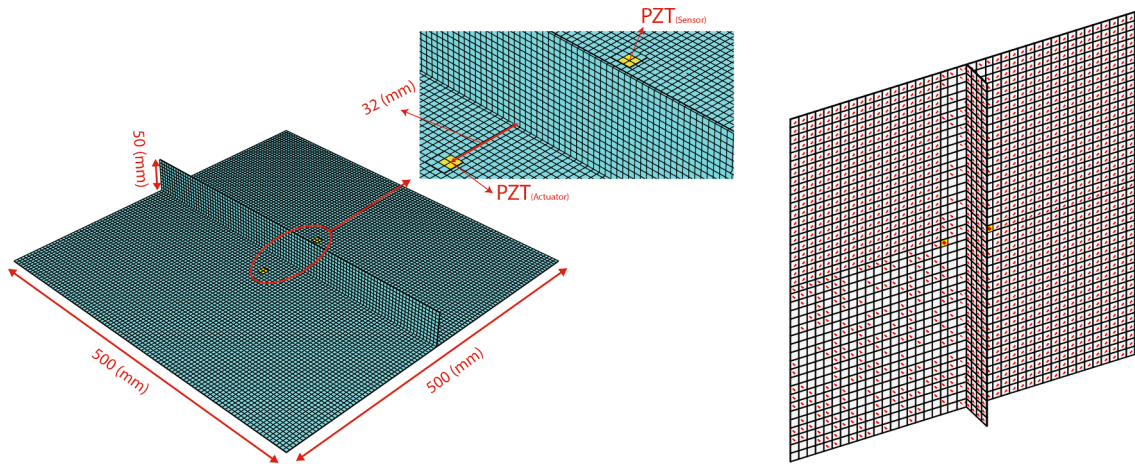
Fig. 14. FEM (left) and SBFEM (right) discretization of the PZT-equipped stiffened plate.
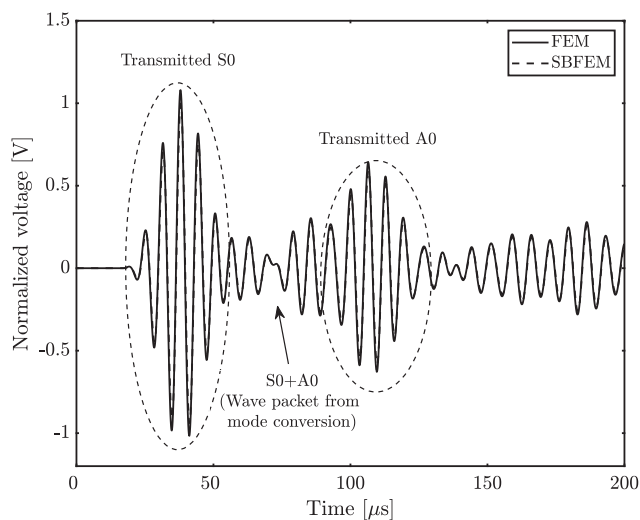

Fig. 15. Voltage of the sensor PWAS receiving the Lamb wave in the stiffened plate modeled using SBFEM and FEM.

Because the FEM model takes into account the electric potential DOF of the PWAS, the data consistency supports the accuracy of the suggested model for PWAS. The SBFEM model has an 8-fold lower DOF than the FE model. The low computational cost of the SBFEM reflects its potential for application in PWAS-based damage identification processes.

7. Conclusions

The application of 3D SBFEM to PWAS-based Lamb wave SHM was investigated in this study. In the context of SBFEM, an effective method for simulating the electromechanical effects of PWAS, which is extensively used in SHM applications, was proposed. The model is based on one-way PWAS-structure interaction and can be simply integrated into SBFEM's elastodynamic equations as an equivalent body load. The semi-discretized equation of SBFEM was solved using the continued fraction approach. The adaptability of mesh generation in SBFEM was leveraged for straightforward discretization of the complex topologies by converting standard finite elements into S-elements. The proposed formulation was used to simulate the Lamb wave health monitoring of a cracked plate, notched plate, and a stiffened plate. The SBFEM's performance was verified using its experimental and FEM counterpart results. In comparison to FEM, the SBFEM demonstrated a fast convergence rate with an improvement as the surface element order was increased. A significant conformity between experimental and SBFEM results proved the SBFEM's capacity to be used in real-application SHM. The great agreement between the results of SBFEM and fully electro-mechanical coupled FEM, confirms the validity of the proposed model for PWAS. The computing effort of the SBFEM is orders of magnitude less than that of the FEM, implying that it has a lot of potential for usage in PWAS-based damage identification procedures. Future work on using SBFEM for stochastic analysis of damage diagnostics is ongoing [69].

Declaration of Competing Interest

The authors declare that they have no known competing financial interests or personal relationships that could have appeared to influence the work reported in this paper.

Data availability

Data will be made available on request.

References

[1] R. Gorgin, Y. Luo, Z. Wu, Environmental and operational conditions effects on Lamb wave based structural health monitoring systems : A review, Ultrasonics 105 (February) (2020), 106114.

[2] Y. Zheng, K. Liu, Z. Wu, D. Gao, R. Gorgin, S. Ma, Z. Lei, Lamb waves and electro-mechanical impedance based damage detection using a mobile PZT transducer set, Ultrasonics 92 (2019) 13–20.

[3] J.B. Ihn, F.K. Chang, Detection and monitoring of hidden fatigue crack growth using a built-in piezoelectric sensor/actuator network: II. Validation using riveted joints and repair patches, Smart Mater. Struct. 13 (3) (2004) 621–630.

[4] D. Wang, J. He, X. Guan, J. Yang, W. Zhang, A model assessment method for predicting structural fatigue life using Lamb waves, Ultrasonics 84 (2018) 319–328.

[5] S. Yuan, J. Chen, W. Yang, L. Qiu, On-line crack prognosis in attachment lug using Lamb wave-deterministic resampling particle filter-based method, Smart Mater. Struct. 26 (8) (2017) pp.

[6] N. Quaegebeur, P.C. Ostiguy, P. Masson, Correlation-based imaging technique for fatigue monitoring of riveted lap-joint structure, Smart Mater. Struct. 23 (5) (2014) 055007.

[7] K. Diamanti, J.M. Hodgkinson, C. Soutis, Detection of low-velocity impact damage in composite plates using lamb waves, Struct. Heal. Monit. 3 (1) (2004) 33–41.

[8] Z. Luo, L. Zeng, J. Lin, J. Hua, A reshaped excitation regenerating and mapping method for waveform correction in Lamb waves dispersion compensation, Smart Mater. Struct. 26 (2) (2017) 025016.

[9] M. Carboni, A. Gianneo, M. Giglio, A Lamb waves based statistical approach to structural health monitoring of carbon fibre reinforced polymer composites, Ultrasonics 60 (2015) 51–64.

[10] C. Höhne, J. Prager, H. Gravenkamp, Computation of dispersion relations for axially symmetric guided waves in cylindrical structures by means of a spectral decomposition method, Ultrasonics 63 (2015) 54–64.

[11] J. Lin, et al., Theoretical and experimental investigation of circumferential guided waves in orthotropic annuli, Ultrasonics 123 (2022), 106715.

[12] P. Packo, P. Kijanka, M.J. Leamy, Spectral analysis of guided wave propagation in discretized domains under local interactions, Proc. Inst. Mech. Eng. Part C J. Mech. Eng. Sci. 234 (3) (2020) 746–769.

[13] Y. Shen, V. Giurgiutiu, Combined analytical FEM approach for efficient simulation of Lamb wave damage detection, Ultrasonics 69 (2016) 116–128.

[14] H. Chen, M. Deng, G. Gao, N. Hu, Y. Xiang, Modeling and simulation of static component generation of Lamb wave propagation in a layered plate, Ultrasonics 116 (May) (2021), 106473.

[15] H. Chen, G. Gao, N. Hu, M. Deng, Y. Xiang, Modeling and simulation of frequency mixing response of two counter-propagating Lamb waves in a two-layered plate, Ultrasonics 104 (February) (2020), 106109.

[16] C. Yang, L. Ye, Z. Su, M. Bannister, Some aspects of numerical simulation for Lamb wave propagation in composite laminates, Compos. Struct. 75 (1–4) (2006) 267–275.

[17] H. Chen, Z. Feng, Y. Du, Q. Chen, H. Miao, Spectral finite element method for efficient simulation of nonlinear interactions between Lamb waves and breathing cracks within the bi-potential framework, Int. J. Mech. Sci., 215 (November 2021) (2022) 106954.

[18] S. Ha, F.K. Chang, Optimizing a spectral element for modeling PZT-induced Lamb wave propagation in thin plates, Smart Mater. Struct. 19 (1) (2010) 015015.

[19] D.M. Joglekar, M. Mitra, Analysis of nonlinear frequency mixing in 1D waveguides with a breathing crack using the spectral finite element method, Smart Mater. Struct. 24 (11) (2015) 115004.

[20] B.C. Lee, W.J. Staszewski, Modelling of Lamb waves for damage detection in metallic structures: Part I. Wave interactions with damage, Smart Mater. Struct. 12 (5) (2003) 815–824.

[21] F. Zou, I. Benedetti, M.H. Aliabadi, A boundary element model for structural health monitoring using piezoelectric transducers, Smart Mater. Struct. 23 (1) (2014) 015022.

[22] X. Wan, G. Xu, Q. Zhang, P.W. Tse, H. Tan, A quantitative method for evaluating numerical simulation accuracy of time-transient Lamb wave propagation with its applications to selecting appropriate element size and time step, Ultrasonics 64 (July) (2016) 25–42.

[23] J. Jingpin, M. Xiangji, H. Cunfu, W. Bin, Nonlinear Lamb wave-mixing technique for micro-crack detection in plates, NDT E Int. 85 (October) (2015, 2017,) 63–71.

[24] W. Ostachowicz, P. Kudela, M. Krawczuk, A. Zak, Guided waves in structures for SHM: the time-domain spectral element method, John Wiley & Sons, 2011.

[25] H. Gravenkamp, A.A. Saputra, C. Song, C. Birk, Efficient wave propagation simulation on quadtree meshes using SBFEM with reduced modal basis, Int. J. Numer. Methods Eng. 110 (12) (2017) 1119–1141.

[26] C. Zhu, G. Lin, J. Li, Modelling cohesive crack growth in concrete beams using scaled boundary finite element method based on super-element remeshing technique, Comput. Struct. 121 (2013) 76–86.

[27] S. Hell, W. Becker, The scaled boundary finite element method for the analysis of 3D crack interaction, J. Comput. Sci. 9 (2015) 76–81.

[28] M.H. Bazyar, C. Song, Time-harmonic response of non-homogeneous elastic unbounded domains using the scaled boundary finite-element method, Earthq. Eng. Struct. Dyn. 35 (3) (2006) 357–383.

[29] C. Li, H. Man, C. Song, W. Gao, Analysis of cracks and notches in piezoelectric composites using scaled boundary finite element method, Compos. Struct. 101 (2013) 191–203.

[30] C. Li, H. Man, C. Song, W. Gao, Fracture analysis of piezoelectric materials using the scaled boundary finite element method, Eng. Fract. Mech. 97 (2013) 52–71.

[31] M.D. Iqbal, C. Birk, E.T. Ooi, H. Gravenkamp, Development of the scaled boundary finite element method for crack propagation modeling of elastic solids subjected to coupled thermo-mechanical loads, Comput. Methods Appl. Mech. Eng. 387 (2021), 114106.

[32] J. Wolf, C. Song, Finite-element modelling of unbounded media, Wiley Chichester, 1997.

[33] H. Man, C. Song, T. Xiang, W. Gao, F. Tin-Loi, High-order plate bending analysis based on the scaled boundary finite element method, Int. J. Numer. Methods Eng. 95 (4) (2013) 331–360.

[34] C.J. Li, Y. Zhang, Y.M. Jia, J. Chen, The polygonal scaled boundary thin plate element based on the discrete Kirchhoff theory, Comput. Math. with Appl. 97 (March) (2021) 223–236.

[35] J. Eisenträger, J. Zhang, C. Song, S. Eisenträger, An SBFEM Approach for Rate-Dependent Inelasticity with Application to Image-Based Analysis, Int. J. Mech. Sci. 182 (April) (2020).

[36] Z. Yin, J. Zhang, F. Yang, W. Ye, J. Liu, G. Lin, An efficient scaled boundary finite element approach in bending and bucking analysis of functionally graded piezoelectric plates, Eng. Anal. Bound. Elem. 132 (August) (2021) 168–181.

[37] H. Gravenkamp, S. Natarajan, Scaled boundary polygons for linear elastodynamics, Comput. Methods Appl. Mech. Eng. 333 (2018) 238–256.

[38] A. Daneshyar, P. Sotoudeh, M. Ghaemian, The scaled boundary finite element method for dispersive wave propagation in higher-order continua, Int. J. Numer. Methods Eng. (2022).

[39] N. Garg, B.G. Prusty, E.T. Ooi, C. Song, G. Pearce, A.W. Phillips, Application of scaled boundary finite element method for delamination analysis of composite laminates using cohesive zone modelling, Compos. Struct. 253 (June) (2020), 112773.

[40] A.L.N. Hirshikesh, R.K. Pramod, E.T. Annabattula, C.S. Ooi, S. Natarajan, Adaptive phase-field modeling of brittle fracture using the scaled boundary finite element method, Comput. Methods Appl. Mech. Eng. 355 (2019) 284–307.

[41] M. Shi, H. Zhong, E.T. Ooi, C. Zhang, C. Song, Modelling of crack propagation of gravity dams by scaled boundary polygons and cohesive crack model, Int. J. Fract. 183 (1) (2013) 29–48.

[42] E.T. Ooi, S. Natarajan, C. Song, E.H. Ooi, Dynamic fracture simulations using the scaled boundary finite element method on hybrid polygon-quadtree meshes, Int. J. Impact Eng. 90 (2016) 154–164.

[43] Z. yuan Li, Z. qiang Hu, G. Lin, J. bo Li, A scaled boundary finite element method procedure for arch dam-water-foundation rock interaction in complex layered half-space, Comput. Geotech., 141(July 2021) (2022) 104524.

[44] S. Pfeil, H. Gravenkamp, F. Duvigneau, E. Woschke, Scaled boundary finite element method for hydrodynamic bearings in rotordynamic simulations, Int. J. Mech. Sci., 199(October 2020) (2021) 106427.

[45] H. Gravenkamp, Efficient simulation of elastic guided waves interacting with notches, adhesive joints, delaminations and inclined edges in plate structures, Ultrasonics 82 (2018) 101–113.

[46] L. Liu, J. Zhang, C. Song, C. Birk, W. Gao, An automatic approach for the acoustic analysis of three-dimensional bounded and unbounded domains by scaled boundary finite element method, Int. J. Mech. Sci. 151 (December) (2018, 2019,) 563–581.

[47] S. Niu, Y. Zhao, H. Bao, Shape sensing of plate structures through coupling inverse finite element method and scaled boundary element analysis, Meas. J. Int. Meas. Confed. 190 (January) (2022), 110676.

[48] N. Sepehry, M. Ehsani, W. Zhu, F. Bakhtiari-Nejad, Application of scaled boundary finite element method for vibration-based structural health monitoring of breathing cracks, J. Vib. Control 27 (23–24) (2021) 2870–2886.

[49] N. Sepehry, F. Bakhtiari-Nejad, W. Zhu, Scaled Boundary Finite Element Method for Modeling of Impedance Based Structural Health Monitoring of 2D Structure, in: ASME 2018 International Design Engineering Technical Conferences and Computers and Information in Engineering Conference, 2018, p. V008T10A034-V008T10A034.

[50] A. Saputra, H. Talebi, D. Tran, C. Birk, C. Song, Automatic image-based stress analysis by the scaled boundary finite element method, Int. J. Numer. Methods Eng. 109 (5) (2017) 697–738.

[51] E.T. Ooi, C. Song, F. Tin-Loi, Z. Yang, Polygon scaled boundary finite elements for crack propagation modelling, Int. J. Numer. Methods Eng. 91 (3) (2012) 319–342.

[52] S. Natarajan, E.T. Ooi, A. Saputra, C. Song, A scaled boundary finite element formulation over arbitrary faceted star convex polyhedra, Eng. Anal. Bound. Elem. 80 (December) (2016, 2017,) 218–229.

[53] D. Zou, K. Chen, X. Kong, J. Liu, An enhanced octree polyhedral scaled boundary finite element method and its applications in structure analysis, Eng. Anal. Bound. Elem. 84 (July) (2017) 87–107.

[54] A. Yaseri, M.H. Bazyar, N. Hataf, 3D coupled scaled boundary finite-element/ finite-element analysis of ground vibrations induced by underground train movement, Comput. Geotech. 60 (2014) 1–8.

[55] S. Ya, S. Eisenträger, C. Song, J. Li, An open-source ABAQUS implementation of the scaled boundary finite element method to study interfacial problems using polyhedral meshes, Comput. Methods Appl. Mech. Eng. 381 (2021), 113766.

[56] V. Giurgiutiu, A. Zagrai, J.J. Bao, Piezoelectric wafer embedded active sensors for aging aircraft structural health monitoring, Struct. Heal. Monit. 1 (1) (2002) 41–61.

[57] C. Song, The Scaled Boundary Finite Element Method, John Wiley & Sons, 2018.

[58] C. Song, J.P. Wolf, The scaled boundary finite-element method—alias consistent infinitesimal finite-element cell method—for elastodynamics, Comput. Methods Appl. Mech. Eng. 147 (3–4) (1997) 329–355.

[59] C. Song, The scaled boundary finite element method in structural dynamics, Int. J. Numer. Methods Eng. 77 (8) (2009) 1139–1171.

[60] A. Daneshyar, M. Ghaemian, A general solution procedure for the scaled boundary finite element method via shooting technique, Comput. Methods Appl. Mech. Eng. 384 (2021), 113996.

[61] D. Chen, C. Birk, C. Song, C. Du, A high-order approach for modelling transient wave propagation problems using the scaled boundary finite element method, Int. J. Numer. Methods Eng. 97 (13) (2014) 937–959.

[62] C. Birk, S. Prempramote, C. Song, An improved continued-fraction-based high-order transmitting boundary for time-domain analyses in unbounded domains, Int. J. Numer. Methods Eng. 89 (3) (2012) 269–298.

[63] C. Li, C. Song, H. Man, E. Tat, W. Gao, 2D dynamic analysis of cracks and interface cracks in piezoelectric composites using the SBFEM, Int. J. Solids Struct. 51 (11–12) (2014) 2096–2108.

[64] H. Man, C. Song, W. Gao, F. Tin-Loi, Semi-analytical analysis for piezoelectric plate using the scaled boundary finite-element method, Comput. Struct. 137 (2014) 47–62.

[65] C. Song, J.P. Wolf, Body loads in scaled boundary finite-element method, Comput. Methods Appl. Mech. Eng. 180 (1–2) (1999) 117–135.

[66] H. Allik, T.J.R. Hughes, Finite element method for piezoelectric vibration, Int. J. Numer. Methods Eng. 2 (2) (1970) 151–157.

[67] S.Y. Wang, A finite element model for the static and dynamic analysis of a piezoelectric bimorph, Int. J. Solids Struct. 41 (15) (2004) 4075–4096.

[68] V. Giurgiutiu, Tuned Lamb wave excitation and detection with piezoelectric wafer active sensors for structural health monitoring, J. Intell. Mater. Syst. Struct. 16 (4) (2005) 291–305.

[69] R. Loendersloot, M. Ehsani, N. Sepehry, M. Shamshirsaz, Numerical Modelling of Stochastic Fatigue Damage Accumulation in Thick Composites, in: European Workshop on Structural Health Monitoring, 2020, pp. 776–787.